

Reynolds number effects on wavelet components of self-preserving turbulent structures

Akira Rinoshika

Department of Mechanical Systems Engineering, Yamagata University, 4-3-16 Jonan, Yonezawa-shi, Yamagata 992-8510, Japan

Yu Zhou

Department of Mechanical Engineering, The Hong Kong Polytechnic University, Hung Hom, Kowloon, Hong Kong

(Received 18 December 2007; revised manuscript received 26 February 2009; published 23 April 2009)

The effect of the Reynolds number on the wavelet-decomposed turbulent structures in a self-preserving plane wake has been investigated for Re_θ (based on the free-stream velocity and momentum thickness, θ , of the wake) = 1350 and 4600. Measurements were made at x/θ (x is the streamwise distance downstream of the cylinder) = 580 for the circular cylinder using two orthogonal arrays of 16 X wires, eight in the (x, y) plane, and eight in the (x, z) plane. A wavelet multiresolution technique is used to analyze the measured hot-wire data. This technique decomposes turbulence structures into a number of components based on their central frequencies, which are linked with the turbulence scales. Sectional streamlines and vorticity contours at the same central frequency, i.e., the comparable scales of turbulent structures, are examined and compared between the two Reynolds numbers. Discernible differences are observed in the turbulent structures of relatively large to intermediate scales. The differences are further quantified in terms of contributions from the turbulent structures of different scales to the Reynolds stresses, vorticity variance, and probability density functions of the fluctuating velocities. The large-scale structure contributes most to the Reynolds stresses and this contribution drops for the higher Re_θ .

DOI: [10.1103/PhysRevE.79.046322](https://doi.org/10.1103/PhysRevE.79.046322)

PACS number(s): 47.27.wb, 47.27.T-, 47.32.ck

I. INTRODUCTION

The effect of the Reynolds number on the near wake, in terms of the mean base pressure, fluctuating lift, vortex formation, and topology [1–5], has been extensively studied with various degrees of detail. This effect is particularly significant in the range of Re_d ($\equiv U_\infty d/\nu$, where U_∞ is the free-stream velocity, d is the cylinder diameter, and ν is the kinematic viscosity of the fluid) = $10^3 \sim 10^4$. The formation length of Kármán vortices and the velocity fluctuation in the shear layer around the cylinder vary greatly with Reynolds number [1]. Instantaneous structures show the generation of small-scale Kelvin-Helmholtz vortices, which are particularly evident at $Re_d=5000$ and even more so at $Re_d=10\,000$ [4]. The effect of the Reynolds number on the far-wake turbulence has also been investigated. Zhou *et al.* [6] found that, for $Re_d=2860 \sim 9750$, a higher Re_d led to an increase in Reynolds stresses and the spatial extent of two-point velocity and vorticity correlation contours.

Rinoshika and Zhou [7] recently developed an orthogonal wavelet multiresolution technique to analyze the turbulent structures for multiple scales in the near wake of a circular cylinder. This technique is capable of tracking the turbulence structures in terms of time and frequencies, and decomposing the turbulence structures into a number of components based on their characteristic frequencies or scales. This analysis differs from the conventional vortex-detection techniques, which could in general extract large-scale vortical structures from turbulence. Using this technique, Rinoshika and Zhou [8,9] studied the effect of initial conditions on the turbulent structures in the near and far wakes. They observed that the most significant contribution to the Reynolds stresses comes from the large- and intermediate-scale structures in the cylinder wake. However, in the screen wake, the contribution to Reynolds stresses comes primarily from the large-scale

structures; the role played by the intermediate-scale structures appears to be less significant than that in the cylinder wake. Their findings suggest a dependence of turbulent intermediate-scale structures, as well as large-scale ones, on the Reynolds number in a self-preserving wake. This is of fundamental significance and has not been previously investigated, thus motivating the present work.

This work aims to apply the orthogonal wavelet multiresolution technique to separate the turbulent structures of different scales and provides both quantitative and qualitative information on the dependence of these structures on the Reynolds number. The velocity data were obtained using 16 X wires in a turbulent far wake generated by a circular cylinder at two Reynolds numbers. Sectional streamlines and vorticity contours of various scales are examined and compared in detail between the two Reynolds numbers. The differences are quantified in terms of the contributions from the turbulence structures of different scales to the Reynolds stresses, vorticity variance, and PDF.

II. EXPERIMENTAL DETAILS

Experiments were conducted in an open-loop low-turbulence wind tunnel with a 2.4 m-long working section (0.35 m \times 0.35 m) in Professor R. A. Antonia's laboratory at The University of Newcastle. The experimental arrangement can be found in Zhou *et al.* [6]. A circular cylinder ($d=6.35$ mm) was installed in the midplane and spanned the full width of the working section, 0.20 m from the exit plane of the contraction. This resulted in a blockage of about 1.8%. Measurements were made at x/θ (x is the streamwise distance downstream of the cylinder and θ is the momentum thickness) = 580 and constant free-stream velocities of $U_\infty = 6.7$ and 23 m/s, which correspond to Reynolds numbers

TABLE I. Characteristic wake parameters.

Re_d	Re_θ	L (mm)	θ (mm)	U_1 (m/s)	U_1/U_∞ (%)	x/d	x/θ
2800	1350	26.1	3.0	0.47	6.9	276	580
9750	4600	26.7	3.0	1.49	6.5	276	580

to illustrate the use of the orthogonal wavelet transform. This wavelet basis is called the Daubechies wavelet basis with an order of 4. Blank entries in Eq. (1) correspond to zeroes.

For a one-dimensional data matrix $V^N = [v_1 \ v_2 \ \dots \ v_{2^N}]^T$, the first transform is performed by the product of two matrices:

$$V_w = C^N V^N = [s_1 \ d_1^N \ s_2 \ d_2^N \ \dots \ s_{2^{N-1}} \ d_{2^{N-1}}^N]^T, \quad (2)$$

where the superscript T denotes a transposed matrix. As evident in the structure of the matrix C^N , two convolution operations are carried out. The odd rows of matrix perform an ordinary convolution with coefficients c_0, c_1, c_2 , and c_3 acting as a low-pass (smoothing) filter, while the even rows perform a different convolution with coefficients $c_3, -c_2, c_1$, and $-c_0$ acting as a high-pass (difference) filter. The resulting first transform coefficient matrix, V_w , consists of interlaced smooth and difference coefficients, denoted by s_i and d_i^N ($i = 1, \dots, 2^{N-1}$). This matrix is then permuted such that the first 2^{N-1} elements are the smooth coefficients s_i and the last 2^{N-1} elements are the difference coefficients d_i^N by premultiplying a permuting matrix P^N :

$$V_w^N = P^N V_w = [s_1 \ s_2 \ \dots \ s_{2^{N/2}} \ d_1^N \ d_2^N \ \dots \ d_{2^{N/2}}^N]^T. \quad (3)$$

The last 2^{N-1} difference elements of V_w^N , i.e., the d_i^N coefficients, are called the wavelet coefficients at level N .

The wavelet basis matrix C^{N-1} and the permuting matrix P^{N-1} , which are the halves of C^N and P^N , respectively, are then applied to the first 2^{N-1} smooth elements of V_w^N . The 2^{N-2} smooth s coefficients and 2^{N-2} difference d^{N-1} coefficients are generated in this operation, the latter coefficients

corresponding to the wavelet coefficients of the hierarchical level $N-1$. This pyramidal procedure is repeated until the last hierarchical level 1 consisting of two s coefficients is obtained. The procedure is sometimes referred to as a *pyramidal algorithm*. Therefore, the orthogonal discrete wavelet transform can be expressed in matrix form by

$$S = W V^N = \underbrace{[s_1^m, s_2^m]}_{\text{level 1}}, \underbrace{[d_1^2, d_2^2]}_{\text{level 2}}, \underbrace{[d_1^3, d_2^3, d_3^3, d_4^3]}_{\text{level 3}}, \dots, \underbrace{[d_1^N, d_2^N, \dots, d_{2^{N/2}}^N]}_{\text{level N}}]^T, \quad (4)$$

where S and W are discrete wavelet coefficient (or spectrum) matrix and analyzing wavelet matrix of V^N , respectively. In the *pyramidal* operation, W is usually constructed based on a cascade algorithm of an orthogonal wavelet basis function, viz.

$$W = P^1 C^1 \dots P^{N-1} C^{N-1} P^N C^N. \quad (5)$$

In general, wavelet basis functions are chosen such that W satisfies $W^T W = I$, where I is a unit matrix. This condition enables the discrete wavelet transform to be an orthogonal linear operator and invertible. The inverse orthogonal discrete wavelet transform can be simply performed by reversing the procedure, starting with the lowest level of the hierarchy, that is,

$$V^N = W^T S. \quad (6)$$

In this work, the Daubechies wavelet basis with an order of 20, instead of 4, is used since a higher order wavelet basis has good frequency localization and is relatively smooth. Meneveau [12] and Mouri *et al.* [18] examined several orthogonal wavelets (Daubechies, Meyer, Harmonic and LMB) and pointed out that turbulent statistics were essentially independent of the choice of the wavelets. However, the wavelets of lower orders (such as Daubechies wavelet with an order of 2 or Haar) are a poor approximation to an ideal band-pass filter due to its poor frequency-domain characteristics, thus being unsuitable for the analysis of turbulent flow signals [18].

The orthogonal wavelet transform produces coefficients that contain information on the relative local contribution of various frequency bandwidths to the transformed data instead of the frequency components of the original data. In order to obtain the grouped frequency components of the transformed data, the orthogonal wavelet coefficient S is first decomposed into the sum of all levels:

$$\begin{aligned} S &= [s_1^m, s_2^m, d_1^2, d_2^2, d_1^3, d_2^3, d_3^3, d_4^3, \dots, d_1^i, d_2^i, \dots, d_{2^{i/2}}^i, \dots, d_1^N, d_2^N, \dots, d_{2^{N/2}}^N]^T \\ &= [s_1^m, s_2^m, 0, \dots, 0]^T + [0, 0, d_1^2, d_2^2, 0, \dots, 0]^T + [0, 0, 0, 0, d_1^3, d_2^3, d_3^3, d_4^3, 0, \dots, 0]^T \\ &\quad + \dots + [0, \dots, 0, d_1^i, d_2^i, \dots, d_{2^{i/2}}^i, 0, \dots, 0]^T + \dots + [0, \dots, 0, d_1^N, d_2^N, \dots, d_{2^{N/2}}^N]^T \\ &= S_1 + S_2 + S_3 \dots + S_i + \dots + S_N. \end{aligned} \quad (7)$$

The inverse orthogonal wavelet transform is then applied to the coefficient of each level, viz.

$$V^N = W^T S_1 + W^T S_2 + W^T S_3 + \dots + W^T S_i + \dots + W^T S_N, \quad (8)$$

where term $\mathbf{W}^T \mathbf{S}_1$ and $\mathbf{W}^T \mathbf{S}_N$ represent the data components at wavelet level 1 (the lowest grouped frequency) and level N (the highest grouped frequency). This decomposition method is referred to as the wavelet multiresolution technique.

In fact, the wavelet component of each level is calculated using the inverse wavelet transform of the wavelet coefficients at this level, while the wavelet coefficients of other levels are made zero. Furthermore, the sum of all wavelet components can be used to reconstruct the original data given the orthogonal wavelet bases [21].

It is well known that the flow structures are of multiscale and are composed of the high-frequency components of short duration and low-frequency components of long duration. The time-frequency partition resulting from the wavelet multiresolution analysis is long in time when capturing low-frequency structures, thus having good frequency resolution for these structures, and short in time when capturing high-frequency structures, thus having a sharp time resolution for these structures. Therefore, the wavelet multiresolution technique intelligently adapts itself to capture structure features across a wide range of frequencies and provides a natural platform to deal with the time-varying characteristics existing in most real-world time series, which overcomes the limitation of the conventional band-pass filtering technique that has a fixed time-frequency resolution.

It is also worthwhile pointing out that, compared with conventional band-pass filtering techniques, the wavelet components are independent of each other [12,18]. This advantage makes the interpretation of the phenomena more reliable even if the wavelet multiresolution technique is presently just used as a band-pass filtering. In this study, a total of $2^{16}=63\,520$ data points are analyzed using wavelet multiresolution technique and $N=13$ wavelet levels are obtained when using the Daubechies wavelet basis with an order of 20.

B. Vorticity approximation

An instantaneous velocity component V_k can be expressed as the sum of a time-averaging component \bar{V}_k and a fluctuation component v_k , viz.

$$V_k = \bar{V}_k + v_k, \quad (9)$$

where the subscript $k=1, 2,$ and 3 represents the velocity components in the $x, y,$ and z direction, respectively. Using the wavelet multiresolution technique, v_k is decomposed into a number of orthogonal wavelet components based on the central frequencies/wavelet levels. Each wavelet component represents the turbulent structures of a certain range of frequencies. Therefore, the instantaneous velocity of Eq. (9) is rewritten by

$$V_k = \bar{V}_k + \sum_{i=1}^N v_{k,i}, \quad (10)$$

where $v_{k,i}$ is the wavelet component of v_k at the i th wavelet level.

The wavelet component of spanwise vorticity at the i th wavelet level may be approximated by

$$\omega_{zi} = \frac{\partial V_i}{\partial x} - \frac{\partial U_i}{\partial y} = \frac{\partial v_i}{\partial x} - \frac{\partial (\bar{U} + u_i)}{\partial y} \approx \frac{\Delta v_i}{\Delta x} - \frac{\Delta (\bar{U} + u_i)}{\Delta y}, \quad (11)$$

where $U_i = \bar{U} + u_i$ and $V_i \approx v_i$ ($\bar{V} \approx 0$). Apparently, velocity data at eight points in the (x, y) plane may produce spanwise vorticity at each of the seven midpoints between adjacent X wires. In Eq. (11), $\Delta y (\approx 5.0 \text{ mm})$ is spacing between two X wires in the (x, y) plane; $\Delta x = -U_c \Delta t$. Note that Taylor's hypothesis is invoked, which works well for coherent structures, particularly involving isolated structures with no intense interaction such as pairing or tearing. For simplicity, the average convection velocity $U_c = 0.95 U_\infty$ of large-scale vortical structures on the vortex path [5] is used to calculate Δx . Vorticity contours and rms values thus obtained did not show appreciable difference from those obtained using the local mean velocity. Since vorticity is indirectly calculated from velocity signals using the central difference approximation, spacing between X wires may degrade the spatial resolution of vorticity. It could be very difficult to translate reliably this degradation into errors caused due to the scarce of reliable vorticity data for this flow, particularly at a high Re. Nonetheless, the approximation is relatively easy to implement and should be adequate for describing at least the relatively large and intermediate scales of vorticity, thus providing useful qualitative information on comparison between the two Reynolds numbers. As such, it is cautioned that the vorticity estimate for relatively small-scale structures may not be trustworthy.

IV. SPECTRAL CHARACTERISTICS

Figure 1 presents the power spectral density functions, F_v , of the v signal at $y/\theta \approx 5.3$ near the vortex path. The weighted spectrum, fF_v (f is frequency), exhibits the dependence of fluctuating velocity energy on f ; as expected, its slope in the inertial subrange is $-2/3$, irrespective of Re_θ . The most prominent peak in fF_v occurs at Strouhal number $f_0 \theta / U_1 \approx 0.49$ ($f_0 = 75 \text{ Hz}$) for $\text{Re}_\theta = 1350$ and 0.3 ($f_0 = 150 \text{ Hz}$) for $\text{Re}_\theta = 4600$, implying the occurrence of large-

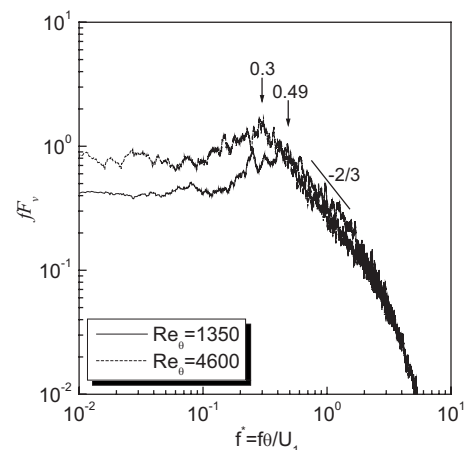


FIG. 1. The v spectrum ($y/\theta \approx 5.3$).

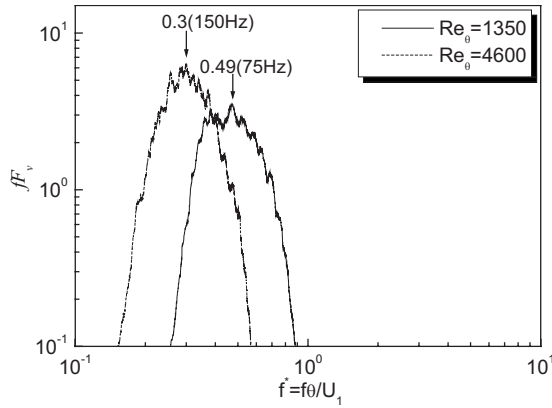


FIG. 2. The v spectrum of the wavelet component at f_0 ($y/\theta \approx 5.3$).

scale vortical structures. The v spectrum displays appreciable difference between the two Reynolds numbers over a range of frequencies around f_0^* , reconfirming the connection between the turbulence memory and large-scale structures [6]. In this study the dominant frequency f_0 of large-scale structures is selected as the “fundamental central frequency” of turbulent structures.

The v signal of 65 536 points at $y/\theta \approx 5.3$ is decomposed into 13 wavelet components using the wavelet multiresolution technique. The spectrum obtained from the Fourier analysis of each wavelet component of the v signal displays a pronounced peak at its central frequency and covers a range of frequencies, as illustrated in Fig. 2 at wavelet level 9 for $Re_\theta=1,350$ and wavelet level 10 for $Re_\theta=4600$, both levels corresponding to the wavelet components of the central frequency f_0 . Table II shows the central frequencies and their bandwidths of the wavelet components from $f_0/2$ to $8f_0$, which cover the range of frequencies that are of major concern in the present investigation. Evidently, the wavelet component of the central frequency f_0 is representative of large-scale vortical structures, and those at a multiple of f_0 and at a frequency smaller than f_0 correspond to smaller-scale and larger-scale structures, respectively. Thus, a comparison between the comparable-scale turbulent structures of the two Reynolds numbers may be reduced to that between the wavelet components of the same multiple of f_0 .

V. RESULTS AND DISCUSSION

A. Instantaneous turbulent structures at different wavelet levels

In order to “visualize” and analyze instantaneous turbulent structures, sectional streamlines and corresponding vorticity contours were constructed from the wavelet components of velocities as well as from measured velocities. The streamlines are viewed in a reference frame translating at the averaged convection velocity of the large-scale structures. To avoid the distortion of flow patterns, the same scales have been used in the x ($=-tU_c$) and y or z directions when plotting streamlines and vorticity contours. The spanwise and lateral vorticity, ω_z and ω_y , are normalized by θ and U_1 . The solid and broken lines in the vorticity contours correspond to positive and negative contours, respectively. For the purpose of comparison, the vorticity contour increment in the (x,y) plane has been made the same as in the (x,z) plane.

Figures 3 and 4 present measured instantaneous sectional streamlines and corresponding normalized vorticity contours for $Re_\theta=1350$ and 4600 in the (x,y) and (x,z) planes. For simplicity, sectional streamlines are called streamlines hereinafter. Large-scale turbulent structures as well as the relatively small-scale ones are identifiable in streamlines. In general, the centers of vortical structures observed in streamlines coincide well with the local vorticity peaks, suggesting that the flow structures may be examined based on either streamlines or vorticity contours. The quasiperiodical structures are evident in the (x,y) plane, though not always so in streamlines or vorticity contours. The sizes of large-scale structures are quite comparable in the two planes. For convenience, the structures in the (x,y) plane are referred to as spanwise structures and those in the (x,z) plane as transverse structures. It would be difficult to examine the Re effect on the behaviors of the structures other than the large-scale ones based on measured streamlines/vorticity contours in Figs. 3 and 4.

Figures 5–8 compare streamlines and the corresponding normalized vorticity contours of different scales in the (x,y) and (x,z) planes between $Re_\theta=1350$ and 4600 , calculated from the wavelet components of velocities at the central frequencies of f_0 and $2f_0$, where f_0 is the same as the dominant vortex frequency. Since the convection velocity U_c of large-scale structures may not be appropriate for relatively small-scale structures, the streamlines of the wavelet component at $8f_0$ were not discussed.

TABLE II. Central frequencies and bandwidths of wavelet components.

Re $_\theta$ =1350			Re $_\theta$ =4600		
Wavelet level	Central frequency (Hz)	Frequency bandwidth (Hz)	Wavelet level	Central frequency (Hz)	Frequency bandwidth (Hz)
8	38 ($f_0/2$)	20–70	9	75 ($f_0/2$)	40–140
9	75 (f_0)	40–140	10	150 (f_0)	70–280
10	150 ($2f_0$)	80–270	11	300 ($2f_0$)	150–550
11	300 ($4f_0$)	110–650	12	600 ($4f_0$)	300–1150
12	600 ($8f_0$)	220–1100	13	1200 ($8f_0$)	600–1750

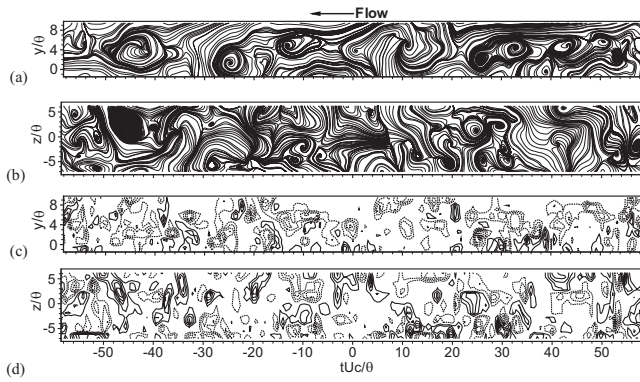


FIG. 3. Measured instantaneous sectional streamlines at $Re_\theta = 1350$: (a) in the (x,y) plane; (b) in the (x,z) plane. Vorticity contours: (c) $\omega_z\theta/U_1$ in the (x,y) plane (Max: 0.05, Min: -0.08 , increment: 0.01); (d) $\omega_y\theta/U_1$ in the (x,z) plane (Max: 0.06, Min: -0.06 , increment: 0.01). Solid and broken lines represent positive and negative contours, respectively. The contour levels of $|\omega_z\theta/U_1| \leq 0.01$ and $|\omega_y\theta/U_1| \leq 0.01$ have been removed. The origin of time is arbitrary.

At f_0 , streamlines and vorticity contours (Figs. 5 and 6) display large-scale structures in the (x,y) and (x,z) planes for both Re_θ . Four and three quasiperiodical vortical structures are clearly identifiable in the (x,y) plane for $Re_\theta = 1350$ and 4600 , respectively. Indeed, these structures correspond well to those identified in the measured streamlines [Figs. 3(a) and 4(a)]. But the structures in Figs. 5(a) and 6(a) appear better organized and more periodical. Furthermore, the flow structure exhibits similarity to the conditionally averaged databased on the detections of large-scale structures [6]. It will be seen in the following section that the wavelet of f_0 contributes most to the turbulent energies, suggesting a correspondence between the wavelet component of the central frequency f_0 and the large-scale vortices. The critical points are readily identifiable in the streamlines, including the foci at the center of spanwise structures, and the saddle

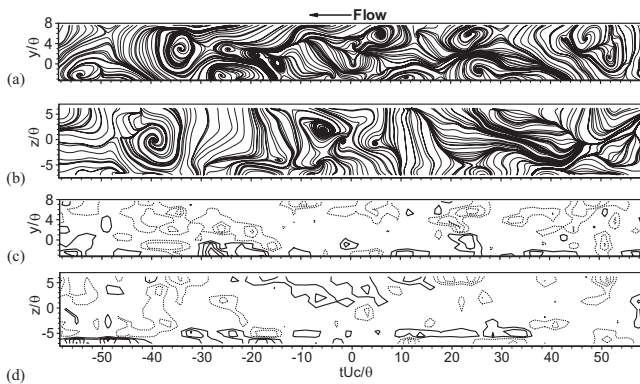


FIG. 4. Measured instantaneous sectional streamlines at $Re_\theta = 4600$: (a) in the (x,y) plane; (b) in the (x,z) plane. Vorticity contours: (c) $\omega_z\theta/U_1$ in the (x,y) plane (Max: 0.04, Min: -0.03 , increment: 0.01); (d) $\omega_y\theta/U_1$ in the (x,z) -plane (Max: 0.05, Min: -0.05 , increment: 0.01). Solid and broken lines represent positive and negative contours, respectively. The contour levels of $|\omega_z\theta/U_1| \leq 0.01$ and $|\omega_y\theta/U_1| \leq 0.01$ have been removed. The origin of time is arbitrary.

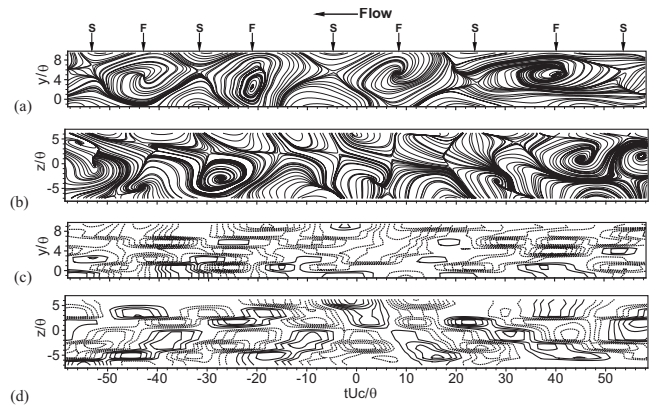


FIG. 5. Sectional streamlines of the wavelet component for f_0 at $Re_\theta = 1350$: (a) in the (x,y) plane; (b) in the (x,z) plane. Vorticity contours: (c) $(\omega_z)_{f_0}\theta/U_1$ in the (x,y) plane (Max: 0.01, Min: -0.018 , increment: 0.002); (d) $(\omega_y)_{f_0}\theta/U_1$ in the (x,z) plane (Max: 0.014, Min: -0.014 , increment: 0.002). Solid and broken lines represent positive and negative contours, respectively. The contour levels of $(\omega_z)_{f_0}\theta/U_1 \leq 0.002$ and $(\omega_y)_{f_0}\theta/U_1 \leq 0.002$ have been removed. The origin of time is arbitrary.

points occurring between spanwise structures. The longitudinal locations of the foci and saddle points are marked by “F” and “S,” respectively, in Figs. 5–10 to facilitate the analysis of turbulent structures. As indicated by the streamlines or vorticity contours, both spanwise and transverse structures are appreciably larger along the streamwise direction at $Re_\theta = 4600$ than at $Re_\theta = 1350$, which conforms with the conditionally averaged results and also two-point velocity or vorticity correlation results [6]. This agreement provides a validation for the present wavelet analysis technique.

The maximum strength of vorticity concentrations is quite comparable between the Reynolds numbers. Furthermore, the strength of spanwise vorticity is comparable to that of transverse vorticity, which results largely from the three di-

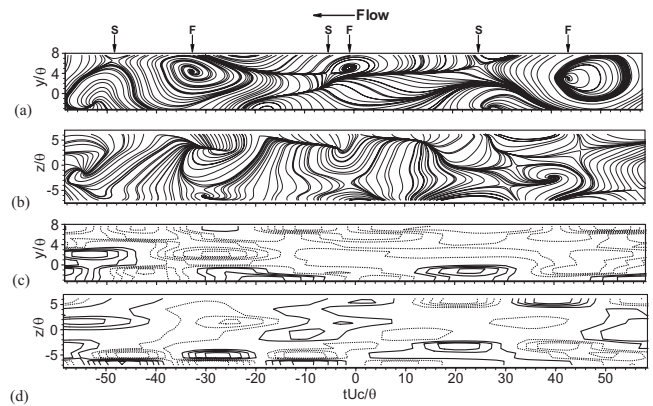


FIG. 6. Sectional streamlines of the wavelet component for f_0 at $Re_\theta = 4600$: (a) in the (x,y) plane; (b) in the (x,z) plane. Vorticity contours: (c) $(\omega_z)_{f_0}\theta/U_1$ in the (x,y) plane (Max: 0.01, Min: -0.014 , increment: 0.002); (d) $(\omega_y)_{f_0}\theta/U_1$ in the (x,z) plane (Max: 0.012, Min: -0.012 , increment: 0.002). Solid and broken lines represent positive and negative contours, respectively. The contour levels of $(\omega_z)_{f_0}\theta/U_1 \leq 0.002$ and $(\omega_y)_{f_0}\theta/U_1 \leq 0.002$ have been removed. The origin of time is arbitrary.

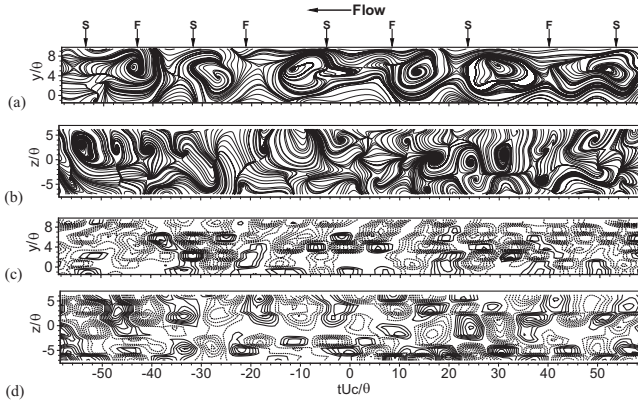


FIG. 7. Sectional streamlines of the wavelet component for $2f_0$ at $Re_\theta=1350$: (a) in the (x,y) plane; (b) in the (x,z) plane. Vorticity contours: (c) $(\omega_z)_{2f_0}\theta/U_1$ in the (x,y) plane (Max: 0.014, Min: -0.026 , increment: 0.002); (d) $(\omega_y)_{2f_0}\theta/U_1$ in the (x,z) plane (Max: 0.022, Min: -0.022 , increment: 0.002). Solid and broken lines represent positive and negative contours, respectively. The contour levels of $(\omega_z)_{2f_0}\theta/U_1 \leq 0.004$ and $(\omega_y)_{2f_0}\theta/U_1 \leq 0.004$ have been removed. The origin of time is arbitrary.

dimensionality of vortical structures. The observation is different from that in the near wake [7], where the spanwise structures are characterized by an appreciably larger maximum of vorticity than the transverse structures. The saddle point always occurs at $(\omega_z)_{f_0}\theta/U_1 \approx 0$ in the (x,y) plane, e.g., at $x/\theta \approx -31$ and $y/\theta \approx 6.0$ in Fig. 5(c); it tends to correspond spatially to the center, at $z/\theta=0$, of a clover-leaf pattern, where $(\omega_y)_{f_0}\theta/U_1 \approx 0$, in the $(\omega_y)_{f_0}\theta/U_1$ contours in the (x,z) plane, e.g., at $tU_c/\theta \approx -31$ and -4 in Fig. 5(d). On the other hand, the focus associated with large-scale structures also corresponds spatially to the center of a clover-leaf pattern of $(\omega_y)_{f_0}\theta/U_1$ at $z/\theta=0$ in the (x,z) plane, e.g., at $tU_c/\theta \approx -44$ and 8 in Fig. 5(d) and $tU_c/\theta \approx 44$ in Fig. 6(d), while

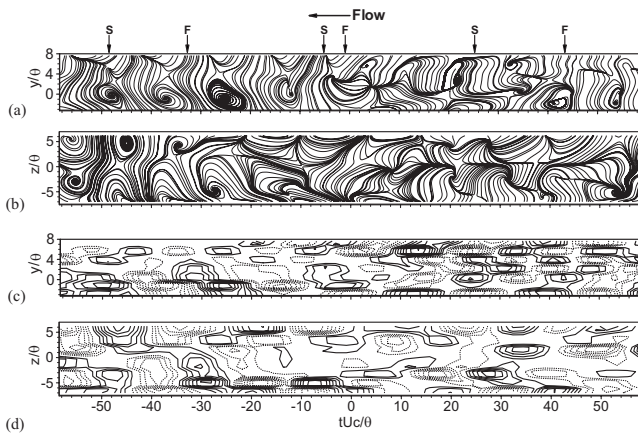


FIG. 8. Sectional streamlines of the wavelet component for $2f_0$ at $Re_\theta=4600$: (a) in the (x,y) plane; (b) in the (x,z) plane. Vorticity contours: (c) $(\omega_z)_{2f_0}\theta/U_1$ in the (x,y) plane (Max: 0.018, Min: -0.018 , increment: 0.002); (d) $(\omega_y)_{2f_0}\theta/U_1$ in the (x,z) plane (Max: 0.02, Min: -0.016 , increment: 0.002). Solid and broken lines represent positive and negative contours, respectively. The contour levels of $(\omega_z)_{2f_0}\theta/U_1 \leq 0.002$ and $(\omega_y)_{2f_0}\theta/U_1 \leq 0.002$ have been removed. The origin of time is arbitrary.

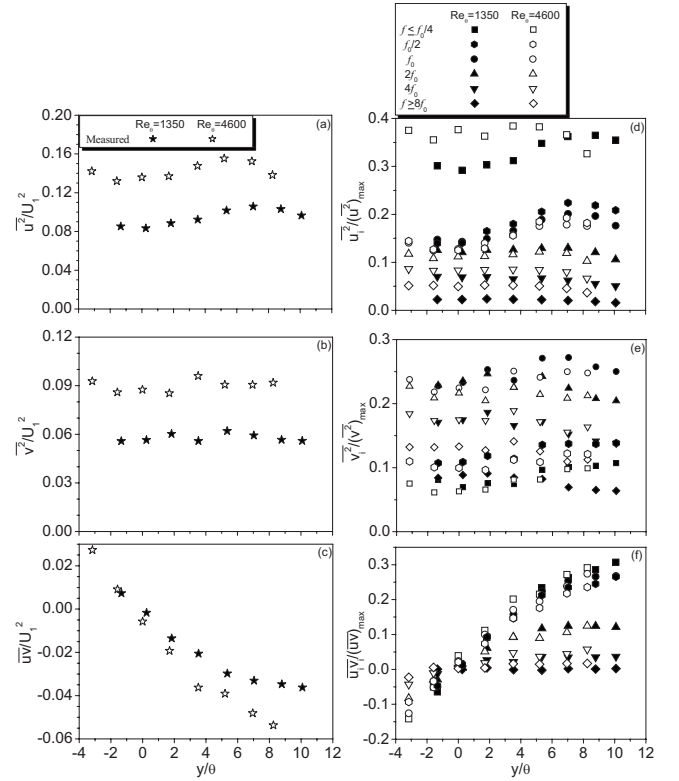


FIG. 9. Velocity variances and Reynolds shear stress of the measured (left) and the wavelet components (right) at various central frequencies.

coinciding well with the local peak of negative $(\omega_z)_{f_0}\theta/U_1$ in the (x,y) plane.

At $Re_\theta=1350$, the ω_z concentrations appear quite comparable, in terms of the maximum vorticity and the contour size, with the ω_y concentrations. But at $Re_\theta=4600$ both ω_z and ω_y concentrations display significantly larger size than at the lower Re_θ . Yiu *et al.* [22] observed appreciable difference in the three components of vorticity as Re_d increased from 2500 to 10 000. This Re_d range is about the same as the present one. The present observation may suggest a memory

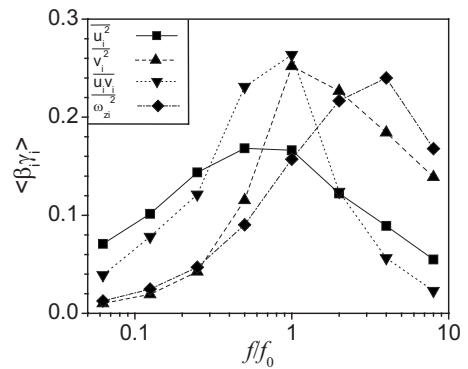


FIG. 10. Dependence of the gross difference ratio $\langle \beta_i \gamma_i \rangle$ on the central frequency between the two Reynolds numbers. The components of lower than $(1/16)f_0$ and higher than $8f_0$ are not included due to very small contributions.

of large-scale structures from the near wake to the far wake, which is consistent with previous reports [10,23].

As the central frequency increases to $2f_0$, the vortical structures (Figs. 7 and 8) occur more frequently but exhibit a smaller size than at f_0 . As at f_0 , streamlines in the (x, z) plane show quite different flow structure from that in the (x, y) plane. The vorticity strength in both planes is larger than that at f_0 . The relatively large structures are evident in the (x, y) plane, e.g., at $tU_c/\theta \approx -42$ and 52 in Fig. 7(a) and at -48 and -37 in Fig. 8(a). Rinoshika and Zhou [7] noted that, in the near wake, the vortical structures in the (x, y) plane associated with the wavelet level at $2f_0$ tend to correspond in location to foci and saddle points associated with the spanwise structures at f_0 [Figs. 5(a) and 6(a)]. This correspondence is however not so good in the present far-wake data. For example, the vortical structures at $tU_c/\theta \approx -44$ for $\text{Re}_\theta = 1350$ [Fig. 7(a)] and $tU_c/\theta \approx -48$ for $\text{Re}_\theta = 4600$ [Fig. 8(a)] correspond to ‘‘F’’ and ‘‘S,’’ respectively. However, the vortical structures at $tU_c/\theta \approx -12$ and -27 for $\text{Re}_\theta = 1350$ [Fig. 7(a)] and $tU_c/\theta \approx -25$ and -37 for $\text{Re}_\theta = 4600$ do not correspond to either ‘‘F’’ or ‘‘S.’’ The observation is probably because the far-wake vortical structures are much less periodic than in the near wake. Furthermore, the vorticity concentrations of opposite sign tend to occur alternately in the longitudinal direction, irrespective of the (x, y) or (x, z) plane. Vorticity concentrations may occur alternately in sign in the spanwise direction, which is consistent with the occurrence of the longitudinal or rib structures [24], for example, at $tU_c/\theta \approx -32$, -10 and 51 for $\text{Re}_\theta = 1350$ in Fig. 7(d) and at $tU_c/\theta \approx 22$ for $\text{Re}_\theta = 4600$ in Fig. 8(d).

Similarly to the wavelet component at f_0 , both ω_z and ω_y concentrations at $\text{Re}_\theta = 4600$ exhibit larger size than at $\text{Re}_\theta = 1350$, though the difference diminishes appreciably compared with that at f_0 . The result suggests that the wavelet component at $2f_0$ also has ‘‘memory’’ from the near wake to the far wake.

Turbulent structures corresponding to the wavelet components at $4f_0$ in both planes (not shown) do not seem to be closely correlated with foci and saddle points associated with the spanwise structures of f_0 . They occur all over the place. In summary, it seems difficult to distinguish, from the structures of the wavelet components at $4f_0$ and higher central frequencies, the turbulent structures in either plane associated with the large-scale spanwise structures and rib structures for both Reynolds numbers. Nevertheless, the vorticity concentrations in the (x, y) and (x, z) planes (not shown) are appreciably stronger at $\text{Re}_\theta = 1350$ than at $\text{Re}_\theta = 4600$; the maximum magnitudes of $(\omega_z)_{4f_0}\theta/U_1$ and $(\omega_y)_{4f_0}\theta/U_1$ are 0.028 and 0.032 at $\text{Re}_\theta = 1350$, respectively, but 0.02 and 0.028 at $\text{Re}_\theta = 4600$. The vorticity strength in the (x, z) plane exceeds that in the (x, y) plane for the two Reynolds numbers, which is similar to that in the near wake [7].

B. Reynolds stresses and vorticity variance

Figures 9(a)–9(c) show the measured Reynolds stresses that are normalized by the centerline velocity deficit U_1 . Evidently, the measured Reynolds stresses at $\text{Re}_\theta = 4600$ exceed considerably their counterparts at $\text{Re}_\theta = 1350$. Table III lists

TABLE III. Maximum values of $\overline{u^2}/U_1^2$, $\overline{v^2}/U_1^2$, \overline{uv}/U_1^2 , and $\overline{\omega_z^2\theta^2}/U_1^2$.

Re_θ	$\overline{u^2}/U_1^2$	$\overline{v^2}/U_1^2$	\overline{uv}/U_1^2	$\overline{\omega_z^2\theta^2}/U_1^2$
1350	0.105	0.064	-0.036	6.3×10^{-8}
4600	0.155	0.096	-0.054	5.1×10^{-8}

the maximum value of the measured time-averaged product $(\beta\gamma)_{\max}$ and vorticity variance, where β and γ represent u , v or ω_z . There is discernible difference in the quantities between the two Reynolds numbers. The observation is agreeable with the previous report [6] of the Reynolds number effect on Reynolds stresses and vorticity variance.

The stresses or vorticity variance associated with a wavelet component may be calculated by [8]

$$\overline{\beta_i\gamma_i} = \frac{1}{n} \sum_{j=1}^n \beta_j\gamma_j, \quad (12)$$

where β_i and γ_i represent u_i , v_i or ω_{z_i} of the i th wavelet component, and $n=63\,520$ is the total number of data points (Sec. III). The calculated $\overline{\beta_i\gamma_i}$ is also normalized by $(\beta\gamma)_{\max}$ to provide a measure of the contribution from each wavelet component, i.e., the turbulent structures of a range of scales, to the Reynolds stresses or vorticity variance.

Figures 9(d)–9(f) show the lateral distributions of $\overline{\beta_i\gamma_i}/(\beta\gamma)_{\max}$ from the lowest to the highest frequency range, as compared with the measured $\overline{\beta\gamma}/(\beta\gamma)_{\max}$ for the two Re_θ . The total contribution from the components of $\frac{1}{2}f_0, f_0, 2f_0, 4f_0$ and higher frequencies accounts for about 62~64% of $\overline{u^2}$, 92~94% of $\overline{v^2}$ and 71~84% of \overline{uv} . These components are reasonably representative of the flow in terms of $\overline{v^2}$, but not so in terms of $\overline{u^2}$ and subsequently \overline{uv} . As a matter of fact, the u spectrum (not shown) exhibits significant energies at frequencies lower than $\frac{1}{2}f_0$. The contribution from the components of central frequencies below $\frac{1}{2}f_0$, as shown in Figs. 9(d) and 9(f), accounts for about 36%~38% of $\overline{u^2}$ and up to 30% of \overline{uv} . This is in distinct contrast with the observation in the near wake ($x/d=20$) of a circular cylinder [8], where contribution from the components of central frequencies below $\frac{1}{2}f_0$, accounts for only about 20% of $\overline{u^2}$ and 15% of \overline{uv} . This difference in the energies of lower frequencies highlights a difference in the turbulence structures between the near and self-preserving wakes, which is connected to the origin of large-scale coherent structures. While one is due to vortex shedding, the other results from shear layer instabilities. On another note, the components of $\frac{1}{2}f_0$ and f_0 contribute about 20% of $\overline{u^2}$ each in the near wake and about the same in the present self-preserving wake. The corresponding contribution from each of the two components to $\overline{v^2}$ is about 40% in the near wake and 25% in the present self-preserving wake, reflecting again the difference in the turbulence structures between the two flows. The $\overline{\beta_i\gamma_i}/(\beta\gamma)_{\max}$ value (Fig. 9) decreases as the central frequency increases from f_0 to higher frequencies, regardless of the Reynolds number, consistent with the perception that lower frequency eddies contain more energy.

The large-scale turbulent structure, i.e., $\overline{\beta_i \gamma_i / (\beta \gamma)}_{\max}$ at $\frac{1}{2}f_0$ and f_0 , makes the largest contribution to the Reynolds stresses, especially in the case of $Re_\theta=1350$. As Re_θ increases from 1350 to 4600, this contribution from the sum of the two wavelet components drops from 43% to 36% to $(\overline{u^2})_{\max}$, 41% to 36% to $(\overline{v^2})_{\max}$ and 53% to 51% to $(\overline{uv})_{\max}$. This result reconfirms Zhou and Antonia's observation [23] that the large-scale vortical structures contribute to the effect of initial conditions.

When the central frequency increases from f_0 to $2f_0$, the decrease in $\overline{\beta_i \gamma_i / (\beta \gamma)}_{\max}$ is rather rapid at $Re_\theta=1350$, from 20% to 13% for $u_i^2 / (\overline{u^2})_{\max}$, from 27% to 24% for $v_i^2 / (\overline{v^2})_{\max}$, and from 27% to 13% for $u_i v_i / (\overline{uv})_{\max}$. In the case of $Re_\theta=4600$, however, the $\overline{\beta_i \gamma_i / (\beta \gamma)}_{\max}$ values at f_0 and $2f_0$ are quite comparable, changing from 19% at f_0 to 12% at $2f_0$ in $u_i^2 / (\overline{u^2})_{\max}$, from 25% at f_0 to 23% at $2f_0$ in $v_i^2 / (\overline{v^2})_{\max}$, and from 27% at f_0 to 13% at $2f_0$ in $u_i v_i / (\overline{uv})_{\max}$. Apparently, the wavelet component of f_0 accounts for considerably more to $\overline{\beta_i \gamma_i / (\beta \gamma)}_{\max}$ at the lower Re_θ than at the higher Re_θ ; however, the wavelet components of $2f_0$ at the two Re_θ make comparable contribution to Reynolds stresses.

As the central frequency increases to $4f_0$, the wavelet components, $\overline{\beta_i \gamma_i / (\beta \gamma)}_{\max}$, further decrease for both Re_θ , though the ratio increases slightly from 7% to 9% to $(\overline{u^2})_{\max}$, 17% to 19% to $(\overline{v^2})_{\max}$, and 4% to 6% to $(\overline{uv})_{\max}$ from $Re_\theta=1350$ to 4600.

Once the central frequency exceeds $4f_0$, the wavelet components $\overline{\beta_i \gamma_i / (\beta \gamma)}_{\max}$ fall off rather rapidly, down to about 2~5% of $(\overline{u^2})_{\max}$, 8~14% of $(\overline{v^2})_{\max}$, and 0.4~2% of $(\overline{uv})_{\max}$ for the sum of all the wavelet components of higher than $4f_0$ and are again quite comparable between the two Reynolds numbers. The observation indicates that the wavelet components of higher central frequencies (or relatively

smaller scales) contribute little to the observed Reynolds number effect.

In summary, the Reynolds stresses of large-scale turbulent structures, i.e., the wavelet components around f_0 , at the higher Re_θ are in general smaller than at the lower Re_θ ; but the Reynolds stresses of small-scale turbulent structures, i.e., the wavelet components of $4f_0$ and higher, become larger at the higher Re_θ . This is consistent with the notion that the separation of turbulence scales increases with Re_θ .

It is of fundamental interest to provide a complete picture on how the wavelet components of different central frequencies contribute to the observed difference in the Reynolds stresses and vorticity variance between the two Reynolds numbers. As such, define a gross difference ratio $\langle \beta_i \gamma_i \rangle$, namely,

$$\langle \beta_i \gamma_i \rangle = \frac{\sum_{j=1}^8 [(\overline{\beta_i \gamma_i})_{Re\theta 2} - (\overline{\beta_i \gamma_i})_{Re\theta 1}]}{\sum_{j=1}^8 [(\overline{\beta \gamma})_{Re\theta 2} - (\overline{\beta \gamma})_{Re\theta 1}]}, \quad (13)$$

where j corresponds to the X-wire number or the lateral position where velocity signals were obtained (Sec. II), i indicates the wavelet level, and subscripts $Re_{\theta 1}$ and $Re_{\theta 2}$ refer to $Re_\theta=4600$ and 1350, respectively. Evidently,

$$\sum_{i=1}^N \langle \beta_i \gamma_i \rangle = \frac{\sum_{i=1}^N \sum_{j=1}^8 [(\overline{\beta_i \gamma_i})_{Re\theta 2} - (\overline{\beta_i \gamma_i})_{Re\theta 1}]}{\sum_{j=1}^8 [(\overline{\beta \gamma})_{Re\theta 2} - (\overline{\beta \gamma})_{Re\theta 1}]} = 100\%, \quad (14)$$

where $N=13$ is the total number of wavelet levels (Sec. III). The ratio defined in Eq. (13) provides a good measure for the contribution from one wavelet level to the spatially averaged difference in the Reynolds stresses or vorticity variance between the two Reynolds numbers. Figure 10 shows the dependence of this ratio on the central frequency, where the components of lower than $(1/16)f_0$ and higher than $8f_0$ are not included due to their very small contributions. If we arbitrarily set a cutoff value of 10% as appreciable contribution, then the wavelet components of the central frequencies at $(1/8)f_0$ through $2f_0$ are predominantly responsible for the spatially averaged difference in the measured $\overline{u^2}$ between the two Reynolds numbers, accounting for 70%. Note that $\langle u_i^2 \rangle$ is almost unchanged from $\frac{1}{2}f_0$ to f_0 , around 17%, and drops appreciably once the central frequency exceeds f_0 , following approximately a log function. The sum of the contributions from the components of $8f_0$ accounts for only about 5%. On the other hand, $\langle v_i^2 \rangle$ increases significantly from $\frac{1}{2}f_0$ to f_0 , reaching the maximum of 25%, and then retreats, also following approximately a log function. The components of $\frac{1}{2}f_0$ through $8f_0$ contribute around 92% to the spatially averaged difference in the measured $\overline{v^2}$. As for $\langle u_i v_i \rangle$, the largest contribution comes from the wavelet components of $\frac{1}{2}f_0$ and f_0 , and falls off rather rapidly as the central frequency increases beyond f_0 . The wavelet components of $\frac{1}{4}f_0$ through $2f_0$, i.e.,

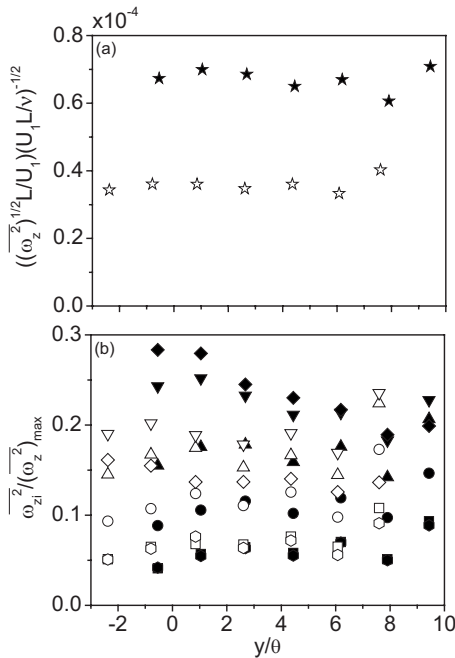


FIG. 11. Measured vorticity variance and wavelet components at various central frequencies. The symbols are the same as in Fig. 9.

large-scale turbulent structures, account for 74% to the difference in the measured \overline{uv} . It may be concluded that the wavelet components of the central frequencies at $(1/8)f_0$ through $2f_0$ (i.e., large-scale turbulent structures) are predominantly responsible for the difference in the measured $\overline{u^2}$ between the two Reynolds numbers. Yet, it is the wavelet components of $\frac{1}{2}f_0$ through $8f_0$ (i.e., large-, intermediate- and relatively small-scale turbulent structures) that contribute most to the difference in the measured $\overline{v^2}$, and the wavelet components of $\frac{1}{4}f_0$ through $2f_0$ (i.e., large-scale turbulent structures) that account most to the difference in the measured \overline{uv} .

Figure 11 presents the measured spanwise vorticity variance, $[(\overline{\omega_z^2})^{1/2}L/U_1](U_1L/\nu)^{-1/2}$, and the wavelet components, $\overline{\omega_{zi}^2}/(\overline{\omega_z^2})_{\max}$. See Table III for the values of $(\overline{\omega_z^2})_{\max}$. The measured vorticity variance at $Re_\theta=1350$ is larger than that of $Re_\theta=4600$. The variation in $\overline{\omega_{zi}^2}/(\overline{\omega_z^2})_{\max}$ with y/θ is qualitatively similar to $\overline{\omega_z^2}/(\overline{\omega_z^2})_{\max}$. The wavelet components of $\frac{1}{2}f_0$ and higher central frequencies account for about 90% of measured vorticity, and those of central frequencies lower than $\frac{1}{2}f_0$ make about 10%. The component of $\frac{1}{2}f_0$ contributes least to the vorticity variance with a percentage of less than 9%, irrespective of the Reynolds number. The next smallest is the component at f_0 , accounting for 15% at $Re_\theta=1350$ and less than 17% of the total vorticity variance at $Re_\theta=4600$. The component at $4f_0$ is responsible for about 22% at $Re_\theta=1350$, and 19% at $Re_\theta=4600$. The wavelet components of $8f_0$ and higher frequencies make the largest contribution to the vorticity variance, accounting for about 28%, at $Re_\theta=1350$, but decreases at $Re_\theta=4600$, compared with the wavelet component of $4f_0$. The observation is in general consistent with the fact that vorticity is largely due to small-scale turbulence structures [25]. The drop in $\overline{\omega_{zi}^2}/(\overline{\omega_z^2})_{\max}$ from the wavelet component of $4f_0$ to those of higher frequencies at $Re_\theta=4600$ is ascribed to the inadequate resolution, both spatially and temporally, for vorticity in present measurement, which deteriorates at higher Re_θ . Therefore, the vorticity data beyond $4f_0$ are not trustworthy.

The wavelet component $\overline{\omega_{zi}^2}/(\overline{\omega_z^2})_{\max}$ tends to be larger at $Re_\theta=1350$ than at $Re_\theta=4600$ in the region $y/\theta < 7.9$. The dependence of the gross difference ratio, $\langle \omega_i^2 \rangle$, on the central frequency is included in Fig. 10. In distinct contrast with the case of Reynolds stresses, $\langle \omega_i^2 \rangle$ arises with higher central frequencies if the data point for $8f_0$ is excluded, suggesting that the difference in vorticity variance between the two Reynolds numbers is more attributed to the wavelet components of higher central frequencies or the relatively small-scale turbulence structures.

VI. CONCLUSION

The effects of the Reynolds number on the turbulent structures of various scales are examined. A wavelet multi-

resolution technique is applied to decompose the measured velocity signals, obtained in the self-preserving wakes at two different Reynolds numbers, into a number of components based on central frequencies, which are linked with the scales of turbulent structures. With the dominant vortex frequency, f_0 , selected to be the base frequency, the wavelet components at the same multiple of f_0 are compared between the two Reynolds numbers, thus allowing the turbulent structures to be compared at different scales between the Reynolds numbers. The following conclusions can be drawn:

(1) The Reynolds number effect is reflected in streamlines and vorticity concentrations and is mainly due to the wavelet components of f_0 and $2f_0$. It is difficult to distinguish the difference in the wavelet components of $4f_0$ and higher central frequencies between the two Reynolds numbers.

(2) The effect of Reynolds number is quite appreciable in terms of Reynolds stresses, largely due to the relatively large-scale turbulent structures, in the present self-preserving wake, conforming to previous reports. First, the Reynolds stresses of large-scale turbulent structures (i.e., the wavelet components around f_0) at the higher Re_θ are in general smaller than at the lower Re_θ ; but the Reynolds stresses of relatively small-scale turbulent structures (the wavelet components of $4f_0$) and higher become larger at the higher Re_θ , consistent with the notion that the separation of turbulence scales increases with Re_θ . Second, the wavelet components of the central frequencies at $(1/8)f_0$ through $2f_0$, i.e., large-scale turbulent structures, are predominantly responsible for the difference in the measured $\overline{u^2}$ between the two Reynolds numbers, accounting for 70%. Yet, it is the wavelet components of $\frac{1}{2}f_0$ through $8f_0$, i.e., large- and intermediate-scale turbulent structures, that contribute most, around 92%, to the difference in the measured $\overline{v^2}$, and the wavelet components of $\frac{1}{4}f_0$ through $2f_0$, i.e., large-scale turbulent structures, that account for most (74%) to the difference in the measured \overline{uv} .

(3) There is a difference in the estimated vorticity variance between the Reynolds numbers. In contrast to the Reynolds stresses, the wavelet components of higher central frequencies, in particular those at and exceeding f_0 , or the smaller turbulence structures contribute more to this difference. The highest contribution is from the wavelet component of $4f_0$.

ACKNOWLEDGMENTS

The experiments were conducted at Professor R. A. Antonia's laboratory at The University of Newcastle with the financial support from Australian Research Council. A.R. acknowledges support by Grant-in-Aid for Scientific Research (C) (Grant No. 17560136) from Japanese Society for the Promotion of Science. Y.Z. is grateful for support given to him by the Research Grants Council of the Government of the HKSAR through Grant No. PolyU 5334/06E.

- [1] J. H. Gerrard, *J. Fluid Mech.* **22**, 187 (1965).
- [2] A. Roshko and W. Fiszdon, *Problems of Hydrodynamics and Continuum Mechanics* (SIAM, Philadelphia, PA, 1969), pp. 606–616.
- [3] B. Cantwell and D. Coles, *J. Fluid Mech.* **136**, 321 (1983).
- [4] J. C. Lin, J. Towfighi, and D. Rockwell, *J. Fluids Structures* **9**, 409 (1995).
- [5] J. F. Huang, Y. Zhou, and T. Zhou, *Exp. Fluids* **40**, 884 (2006).
- [6] Y. Zhou, R. A. Antonia, and W. K. Tsang, *Exp. Fluids* **25**, 118 (1998).
- [7] A. Rinoshika and Y. Zhou, *J. Fluid Mech.* **524**, 229 (2005).
- [8] A. Rinoshika and Y. Zhou, *Phys. Rev. E* **71**, 046303 (2005).
- [9] A. Rinoshika and Y. Zhou, *Int. J. Heat Fluid Flow* **28**, 948 (2007).
- [10] I. Wygnanski, F. Champagne, and B. Marasli, *J. Fluid Mech.* **168**, 31 (1986).
- [11] M. Yamada and K. Ohkitani, *Prog. Theor. Phys.* **86**, 815 (1991).
- [12] C. Meneveau, *J. Fluid Mech.* **232**, 469 (1991).
- [13] M. Farge, *Annu. Rev. Fluid Mech.* **24**, 395 (1992).
- [14] H. Li and T. Nozaki, *JSME Int. J., Ser. B* **38**, 525 (1995).
- [15] H. Li, *ASME J. Fluids Eng.* **120**, 778 (1998).
- [16] M. Farge, K. Schneider, and N. Kevlahan, *Phys. Fluids* **11**, 2187 (1999).
- [17] M. Farge, G. Pellegrino, and K. Schneider, *Phys. Rev. Lett.* **87**, 054501 (2001).
- [18] H. Mouri, H. Kubotani, T. Fujitani, H. Niino, and M. Takaoka, *J. Fluid Mech.* **389**, 229 (1999).
- [19] H. Li, M. Takei, M. Ochi, Y. Saito, and K. Horii, *Trans. Jpn. Soc. Aeronaut. Space Sci.* **42**, 127 (1999).
- [20] H. Li, H. Hu, T. Kobayashi, T. Saga, and N. Taniguchi, *AIAA J.* **40**, 1037 (2002).
- [21] S. Mallat, *A Wavelet Tour of Signal Processing* (Academic Press, New York, 1998).
- [22] M. W. Yiu, Y. Zhou, T. Zhou, and L. Cheng, *AIAA J.* **42**, 1009 (2004).
- [23] Y. Zhou and R. A. Antonia, *Exp. Fluids* **19**, 112 (1995).
- [24] J. F. Huang, Y. Zhou, and T. Zhou, *Exp. Fluids* **40**, 884 (2006).
- [25] T. Zhou, Y. Zhou, M. W. Yiu, and L. P. Chua, *Exp. Fluids* **35**, 459 (2003).